

Our experiments thus far do not clearly distinguish between these two interesting scenarios; they have, however, unveiled a previously unknown route to complex structures such as the honeycomb and kagome lattices: self-assembly of magnetic molecules that carry electric dipole moments (30). The data also indicate that inclusion of a JT-inactive, oxygen-coordinated transition metal ion (here  $\text{SbO}_6$ ) favors spin-orbital entanglement over a conventional cooperative static JT-phase transition. An unexpected outcome is the response to nanoscale disorder. Rather than forming a glassy state as in typical geometrically frustrated magnets, the spin-orbital quantum state in  $\text{Ba}_3\text{CuSb}_2\text{O}_9$  is robust within linked nanoscale domains. A key question to be addressed through theory and experiments is whether a short-range dynamic spin-orbital state is a property of the bulk decorated honeycomb lattice or contingent on linked nanoscale structural domains.

### References and Notes

1. P. A. Lee, *Science* **321**, 1306 (2008).
2. L. Balents, *Nature* **464**, 199 (2010).
3. S. Sachdev, *Phys. Rev. B* **45**, 12377 (1992).
4. X.-G. Wen, *Phys. Rev. B* **65**, 165113 (2002).
5. H. Morita, S. Watanabe, M. Imada, *J. Phys. Soc. Jpn.* **71**, 2109 (2002).
6. A. Kitaev, *Ann. Phys.* **321**, 2 (2006).
7. J. S. Helton *et al.*, *Phys. Rev. Lett.* **98**, 107204 (2007).

8. Y. Shimizu, K. Miyagawa, K. Kanoda, M. Maesato, G. Saito, *Phys. Rev. Lett.* **91**, 107001 (2003).
9. T. Itou, A. Oyamada, S. Maegawa, M. Tamura, R. Kato, *Phys. Rev. B* **77**, 104413 (2008).
10. M. Yamashita *et al.*, *Science* **328**, 1246 (2010).
11. G. H. Wannier, *Phys. Rev.* **79**, 357 (1950).
12. Supplementary material is available on Science Online.
13. V. P. Köhl, *Z. Anorg. Allg. Chem.* **442**, 280 (1978).
14. H. D. Zhou *et al.*, *Phys. Rev. Lett.* **106**, 147204 (2011).
15. J. Kaneshiro, S. Kawado, H. Yokota, Y. Uesu, T. Fukui, *J. Appl. Phys.* **104**, 054112 (2008).
16. F. S. Ham, *Phys. Rev.* **166**, 307 (1968).
17. M. Enderle *et al.*, *Europhys. Lett.* **70**, 237 (2005).
18. P. Schiffer, I. Daruka, *Phys. Rev. B* **56**, 13712 (1997).
19. A. J. Willans, J. T. Chalker, R. Moessner, *Phys. Rev. Lett.* **104**, 237203 (2010).
20. T. Aharen *et al.*, *Phys. Rev. B* **81**, 224409 (2010).
21. J. P. Carlo *et al.*, *Phys. Rev. B* **84**, 100404 (2011).
22. Y. Doi, Y. Hinatsu, K. Ohoyama, *J. Phys. Condens. Matter* **16**, 8923 (2004).
23. D. S. Fisher, *Phys. Rev. B* **50**, 3799 (1994).
24. L. F. Feiner, A. Oleś, J. Zaanen, *Phys. Rev. Lett.* **78**, 2799 (1997).
25. Y. Q. Li, M. Ma, D. N. Shi, F. C. Zhang, *Phys. Rev. Lett.* **81**, 3527 (1998).
26. F. Vernay, K. Penc, P. Fazekas, F. Mila, *Phys. Rev. B* **70**, 014428 (2004).
27. F. Reynaud *et al.*, *Phys. Rev. Lett.* **86**, 3638 (2001).
28. V. Fritsch *et al.*, *Phys. Rev. Lett.* **92**, 116401 (2004).
29. J. Nasu, A. Nagano, M. Naka, S. Ishihara, *Phys. Rev. B* **78**, 024416 (2008).
30. B. D. Metcalf, *Phys. Lett. A* **46**, 325 (1974).

**Acknowledgments:** We thank Y. Uesu, J. Kaneshiro, and H. Yokota for scanning SHG microscope measurements; Y. Kiuchi for ICP analysis; T. Nakano and Y. Nozue for X-band ESR measurements; and V. Thampy for assistance in

neutron-scattering data analysis. We are also grateful for fruitful discussions with N. Drichko, Z. Hao, D. Hamane, S. Ishihara, M. Isobe, T. M. McQueen, T. Mizokawa, Y. Nakanishi, N. Nagaosa, S. Onoda, K. Takada, O. Tchernyshyov, Y. Wakabayashi, and J. Yamaura. This work is partially supported by Grants-in-Aid for Scientific Research from Japan Society for the Promotion of Science (JSPS) (nos. 20340089, 21684019, and 23244074) and from Ministry of Education, Culture, Sports, Science, and Technology (MEXT) on Priority Areas (nos. 19051010, 19051015, and 19052003), by Global Centers of Excellence (COE) programs “the Physical Sciences Frontier” and “Core Research and Engineering Science of Advanced Materials” MEXT, by a Toray Science and Technology grant, and by the U.S.-Japan Cooperative Program, ISSP. Work at IQM was supported by U.S. Department of Energy (DOE), Office of Basic Energy Sciences, Division of Materials Sciences and Engineering under award DE-FG02-08ER46544. This work used facilities supported in part by the NSF (no. DMR-0944772). Part of this work was conducted while C.B. was a JSPS fellow at ISSP. The x-ray diffraction experiments were carried out at SPring-8 (Super Photon ring-8 GeV). The EXAFS experiments were carried out at Stanford Synchrotron Radiation Lightsource, supported by DOE. Muon spin relaxation experiments were performed at TRIUMF (Canada’s national laboratory for particle and nuclear physics).

### Supplementary Materials

[www.sciencemag.org/cgi/content/full/336/6081/559/DC1](http://www.sciencemag.org/cgi/content/full/336/6081/559/DC1)  
Materials and Methods  
Supplementary Text  
Figs. S1 to S7  
Tables S1 and S2  
References (31–41)

3 August 2011; accepted 9 March 2012  
10.1126/science.1212154

# Anisotropic Energy Gaps of Iron-Based Superconductivity from Intraband Quasiparticle Interference in LiFeAs

M. P. Allan,<sup>1,2,3\*</sup> A. W. Rost,<sup>2,3\*</sup> A. P. Mackenzie,<sup>3</sup> Yang Xie,<sup>2</sup> J. C. Davis,<sup>1,2,3,4†</sup> K. Kihou,<sup>5,6</sup> C. H. Lee,<sup>5,6</sup> A. Iyo,<sup>5,6</sup> H. Eisaki,<sup>5,6</sup> T.-M. Chuang<sup>1,2,7†</sup>

If strong electron-electron interactions between neighboring Fe atoms mediate the Cooper pairing in iron-pnictide superconductors, then specific and distinct anisotropic superconducting energy gaps  $\Delta_i(\vec{k})$  should appear on the different electronic bands  $i$ . Here, we introduce intraband Bogoliubov quasiparticle scattering interference (QPI) techniques for determination of  $\Delta_i(\vec{k})$  in such materials, focusing on lithium iron arsenide (LiFeAs). We identify the three hole-like bands assigned previously as  $\gamma_1$ ,  $\alpha_2$ , and  $\alpha_1$ , and we determine the anisotropy, magnitude, and relative orientations of their  $\Delta_i(\vec{k})$ . These measurements will advance quantitative theoretical analysis of the mechanism of Cooper pairing in iron-based superconductivity.

In typical FeAs-based materials, every second As atom lies above or below the FeAs layer (Fig. 1A) so that the crystallographic unit cell, instead of being a square with an Fe atom at each corner (Fig. 1A, dashed box), is rotated by  $45^\circ$  and has an As at each corner (Fig. 1A, solid box). The corresponding momentum space ( $\vec{k}$ -space) Brillouin zone then contains five electronic bands; the hole-like  $\alpha_1$ ,  $\alpha_2$ , and  $\gamma$  bands surround the  $\Gamma$  point, and the electron-like  $\beta_1$  and  $\beta_2$  bands surround the  $\tilde{M}$  point (Fig. 1B). The superconductivity derives ( $I$ ) from a commensurate antiferromagnetic and orthorhombic “parent” state [see

supplementary materials (2)]. The highest superconducting critical temperatures ( $T_c$ ) occur when the magnetic and structural transitions are suppressed toward zero temperature. Theories describing the FeAs superconductivity can be quite complex ( $I$ , 3–9), but they typically contain two essential ingredients: (i) the predominant superconducting order parameter (OP) symmetry is  $s_\pm$ , that is, it has  $s$ -wave symmetry but changes sign between different bands; and (ii) the superconducting energy gap functions  $\Delta_i(\vec{k})$  on different bands  $i$  are anisotropic in  $\vec{k}$ -space, with each exhibiting distinct  $90^\circ$  rotational ( $C_4$ ) symmetry

and a specific relationship of gap minima/maxima relative to the BZ axes. Figure 1C shows a schematic of such a situation for just two electronic bands, with contours of constant energy (CCE) for their Bogoliubov quasiparticles shown in Fig. 1D.

Although there is evidence for  $s_\pm$  OP symmetry ( $I$ , 10, 11), the structure of any anisotropic gaps  $\Delta_i(\vec{k})$  on different bands and their relative  $\vec{k}$ -space orientation is an open question for virtually all iron-based superconductors ( $I$ ). However, it is the structure of these  $\Delta_i(\vec{k})$  that is crucial for understanding the pairing interactions. Thermodynamic and transport studies [which cannot reveal  $\Delta_i(\vec{k})$ ] provide good evidence for electronic anisotropy ( $I$ , 12–14). By contrast, almost all  $\vec{k}$ -space angle-resolved photoemission spectroscopy (ARPES) studies of these materials, including LiFeAs ( $I$ ),

<sup>1</sup>Condensed Matter Physics and Materials Science (CMPMS) Department, Brookhaven National Laboratory, Upton, NY 11973, USA. <sup>2</sup>Laboratory of Solid State Physics, Department of Physics, Cornell University, Ithaca, NY 14853, USA. <sup>3</sup>Scottish Universities Physics Alliance (SUPA), School of Physics and Astronomy, University of St Andrews, St Andrews, Fife KY16 9SS, UK. <sup>4</sup>Kavli Institute at Cornell for Nanoscale Science, Cornell University, Ithaca, NY 14853, USA. <sup>5</sup>Institute of Advanced Industrial Science and Technology, Tsukuba, Ibaraki 305-8568, Japan. <sup>6</sup>Japan Science and Technology Agency (JST), Transformative Research-Project on Iron Pnictides (TRIP), Tokyo 102-0075, Japan. <sup>7</sup>Institute of Physics, Academia Sinica, Nankang, Taipei 11529, Taiwan.

\*These authors contributed equally to this work.

†To whom correspondence should be addressed. E-mail: jcdavis@ccmr.cornell.edu (J.C.D.); chuangtm@phys.sinica.edu.tw (T.-M.C.)

have reported the  $\Delta_i(\vec{k})$  to be isotropic in the  $k_x/k_y$  plane (1). Subsequent to our submission, however, nodeless anisotropic gaps with values spanning the range 2 meV  $\rightarrow$  4 meV on the  $\gamma$  band and 5 meV  $\rightarrow$  6 meV on the  $\alpha_2$  band (surrounding  $\Gamma$ ) were reported in LiFeAs (16, 17). For the electron-like pocket at  $\tilde{M}$ , an anisotropic 3 meV  $\rightarrow$  4.5 meV gap is also described, but the reported  $\vec{k}$ -space positions of gap maxima/minima appear mutually inconsistent (16, 17). High-resolution determination of  $\Delta_i(\vec{k})$  should help to more accurately quantify these fundamental characteristics of the superconductivity.

Bogoliubov quasiparticle scattering interference (QPI) imaging is a suitable technique for high-resolution determination of  $\Delta_i(\vec{k})$  (18–24). The scattering interference patterns can be visualized in real space ( $\vec{r}$ -space) using spectroscopic imaging scanning tunneling microscopy (SI-STM) in which the tip-sample differential tunneling conductance  $dI/dV(\vec{r}, E) \equiv g(\vec{r}, E)$  is measured as a function of location  $\vec{r}$  and electron energy  $E$ . However, using QPI to determine the  $\Delta_i(\vec{k})$  of iron-pnictide superconductors may be problematic because (i) the large field-of-view  $g(\vec{r}, E)$  imaging [and equivalent high  $\vec{q}$ -space resolution in

$g(\vec{q}, E)$ ] necessary to obtain  $\Delta_i(\vec{k})$  is technically difficult; (ii) complex overlapping QPI patterns are expected from multiple bands; and (iii) most iron-pnictide compounds exhibit poor cleave-surface morphology. This latter point can be mitigated by using a material with a charge-neutral cleave plane (e.g., 11). An iron-pnictide that satisfies this requirement is LiFeAs (25–28), which has a glide plane between two Li layers [(2), section I].

Bogoliubov QPI can be influenced by a variety of effects in the iron-pnictides (21–24). To explore the expected QPI signatures of the  $\Delta_i(\vec{k})$ , we consider the model two-gap structure in Fig. 1, C and D. Within one band, each energy  $\Delta_1^{\min} \leq E \leq \Delta_1^{\max}$  at which  $\Delta_1(\vec{k}) \doteq E$  picks out eight specific  $\vec{k}$ -space locations  $\vec{k}_j(E)$ . In a generalization of the “octet” model of QPI in copper-based superconductors (18–20), scattering between these  $\vec{k}_j(E)$  should produce interference patterns with the seven characteristic QPI wave vectors  $\vec{q}_1 \dots \vec{q}_7$  shown in Fig. 1D. An equivalent set of QPI wave vectors, but now with different lengths and orientations, would be generated by a different  $\Delta_2(\vec{k})$  on the second band (Fig. 1, C and D, yellow). Thus, conventional octet analysis could

be challenging for a multiband anisotropic superconductor, as many intraband QPI wave vectors coincide near the center of  $\vec{q}$ -space.

To achieve a more robust QPI prediction, we next consider the joint-density-of-states (JDOS) approximation for the whole Bogoliubov quasiparticle spectrum (Fig. 1D). In this case, for  $\Delta_1^{\min} \leq E \leq \Delta_1^{\max}$  within a given band (e.g., red band in Fig. 1, C and D), the tips of the “bananas” still strongly influence QPI because of the enhanced JDOS for scattering between these locations and effects inherent to the structure of the coherence factors. Figure 1E shows  $g(\vec{q}, E = (\Delta_{\max} + \Delta_{\min})/2)$  simulated by calculating the JDOS for a single hole-like band (red band of Fig. 1C) [(2), section II]. Although the JDOS approximation gives an intuitive picture of how  $g(\vec{q}, E)$  relates to regions of high density of states in  $\vec{k}$ -space, the T-matrix formalism is needed for a rigorous description (18–24). In Fig. 1F, we show a T-matrix simulation of  $g(\vec{q}, E = (\Delta_{\max} + \Delta_{\min})/2)$  for equivalent parameters as those in Fig. 1E [(2), section II]. By comparison of Fig. 1, E and F, we see that the two types of simulations are virtually indistinguishable and that the expected octet wave vectors

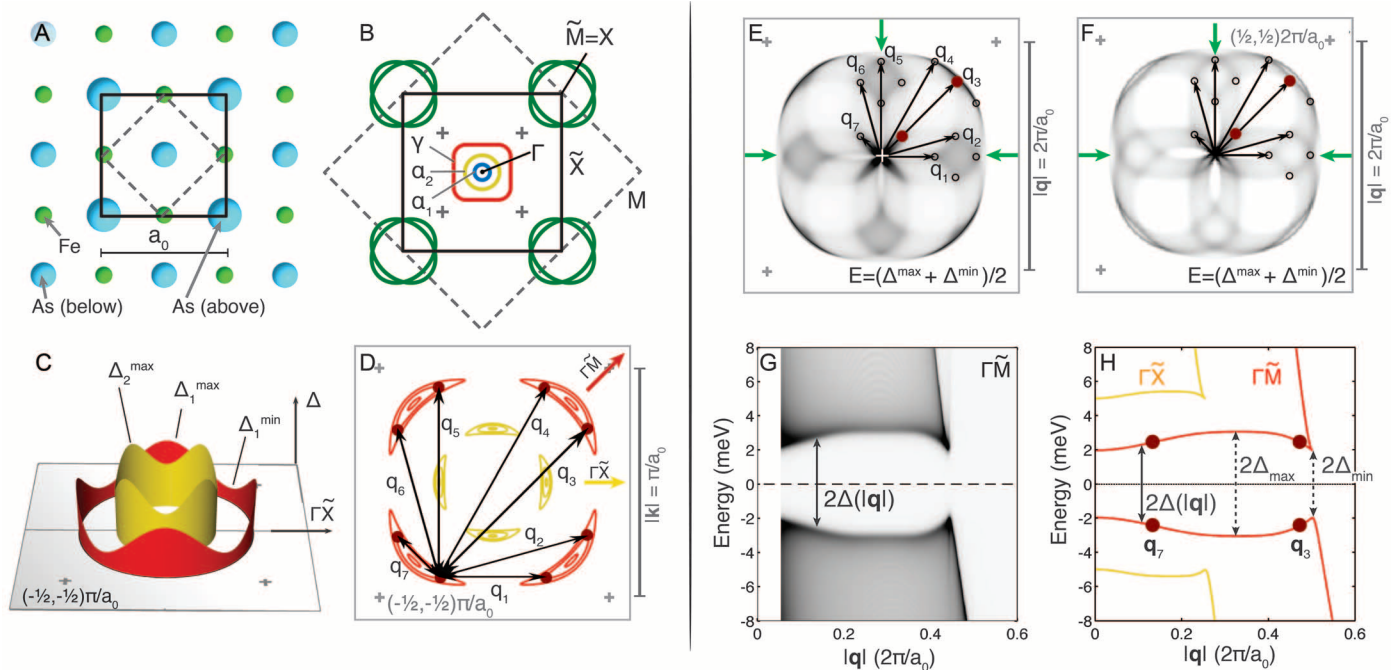


**Fig. 1.** (A) Top view of crystal structure in the FeAs plane. Dashed lines represent the one-Fe unit cell that would exist if all As were coplanar, and the actual unit cell of dimension  $a_0 \approx 0.38$  nm is shown using solid lines. (B) Schematic Fermi surface of an iron-based superconductor like LiFeAs in the tetragonal nonmagnetic Brillouin zone (solid line). The “one-Fe zone” is shown as a dashed line. The blue, yellow, and red curves show the hole-like pockets surrounding the  $\Gamma$  point, and the green curves show electron pockets surrounding the  $\tilde{M}$  point. The gray crosses mark the  $(\pm 1/2, \pm 1/2)\pi/a_0$  points. (C) Model system exhibiting two distinct anisotropic energy gaps  $\Delta_i(\vec{k})$  on two hole-like bands. (D) CCE of the Bogoliubov quasiparticle excitation spectrum for the two bands in (C), each in the same color as its  $\Delta_i(\vec{k})$ . Contours enclose diminishing areas surrounding the gap minimum in each case. Black arrows indicate the octet scattering vectors  $\vec{q}_1 \dots \vec{q}_7$  between the CCE banana tips (red dots). The red and yellow vectors indicate the high-symmetry directions

along which  $g(\vec{q}, E)$  should be measured to determine  $\Delta_i(\vec{k})$  for the respective bands separately; see (H). (E and F) Theoretically simulated  $g(\vec{q}, E = (\Delta_{\max} + \Delta_{\min})/2)$  for a single hole-like band with band- and gap-anisotropy parameters shown in (D), using the JDOS (E) and T-matrix (F) approaches. In  $\vec{q}$ -space, the gray crosses occur at the  $(\pm 1/2, \pm 1/2)2\pi/a_0$  points. The arrows show the scattering vectors  $\vec{q}_1 \dots \vec{q}_7$  from the octet model in (D). The red dots indicate the vectors that lie along  $\Gamma\tilde{M}$ , the direction studied in (G) and (H). (G) JDOS simulation of dependence of scattering intensity in  $g(l\vec{q}, E)$ , with  $\vec{q}$  parallel to  $\Gamma\tilde{M}$  for a single hole-like band with gap anisotropy parameters shown in (C) and (D). Note the curved shapes of scattering intensity maxima, which we then extract in (H). (H) Red curves: Expected trajectory of maxima in scattering intensity  $g(l\vec{q}, E)$  with  $\vec{q}$  parallel to  $\Gamma\tilde{M}$  for  $h_3$ . Yellow curves: Expected maxima in scattering intensity  $g(l\vec{q}, E)$  with  $\vec{q}$  parallel to  $\Gamma\tilde{X}$  for  $h_2$ .



(overlaid by black arrows) are in excellent agreement (as is true for all  $\Delta_1^{\min} \leq E \leq \Delta_1^{\max}$ ). The key QPI signatures of an anisotropic but nodeless  $\Delta_i(\vec{k})$  are therefore expected to be arcs of strong scattering centered along the direction of the gap minima, with regions of minimal scattering intensity located toward the gap maxima (green arrows, Fig. 1, E and F).

The complexity of the simulated  $g(\vec{q}, E)$  (Fig. 1, E and F) also reveals the considerable practical challenges if measured  $g(\vec{q}, E)$  are to be inverted to yield the underlying  $\Delta_i(\vec{k})$ . Therefore, we developed a restricted analysis scheme that still allows the pertinent  $\Delta_i(\vec{k})$  information to be easily extracted. Instead of the usual constant energy  $g(\vec{q}, E)$  images, this approach is based on measuring the maximum scattering intensity in a  $|\vec{q}|$ - $E$  plane along a specific high-symmetry direction—for example,  $\vec{q} \parallel \Gamma\tilde{M}$  for the red band in Fig. 1D. Figure 1G shows a simulation of such a  $|\vec{q}|$ - $E$  intensity plot ( $\vec{q} \parallel \Gamma\tilde{M}$ ) revealing two curved trajectories of maximal scattering intensity. They are extracted and plotted as red curves in Fig. 1H [(2), section III]. Such a plot of intensity maxima in a  $g(\vec{q}, E)$  plane along a high symmetry direction actually contains all the information on  $\Delta(\vec{k})$  for that  $C_4$ -symmetric band. Another band with a different  $\vec{q}$ -space radius and whose gap maxima are rotated by  $45^\circ$  to the first (e.g., yellow in Fig. 1D) can be analyzed similarly; a plot of maxima in  $g(\vec{q}, E)$  for  $\vec{q} \parallel \Gamma\tilde{X}$  (yellow arrow, Fig. 1D) would then yield distinct interference maxima from the  $\Delta(\vec{k})$  of that band (yellow curves, Fig. 1H). The magnitude and relative orientation of  $\Delta_i(\vec{k})$  on mul-

tiple  $C_4$ -symmetric bands of different  $|\vec{q}|$  radius can be determined simultaneously by using this multiband QPI approach. Importantly, the  $\Delta_i(\vec{k})$  are then determined experimentally, not from comparison to simulation but directly from a combination of (i) the measured normal-state band dispersions, (ii) the BZ symmetry, and (iii) the measured geometrical characteristics of the scattering intensity  $g(\vec{q}, E)$  in a specific  $|\vec{q}|$ - $E$  plane [(2), section III].

We implement this approach using LiFeAs crystals with  $T_c \approx 15$  K. Their cleaved surfaces are atomically flat (Fig. 2A) and exhibit the  $a_0 = 0.38$  nm periodicity of either the As or Li layer [(2), section I]. As the glide plane is between Li layers we are probably observing a Li-termination layer. We image  $g(\vec{r}, E)$  with atomic resolution and with a thermal energy resolution  $\delta E \leq 350$   $\mu$ eV at  $T = 1.2$  K. Figure 2A inset shows the spatially averaged differential conductance  $g(E)$  far from in-gap impurity states [(2), section V]. The density of electronic states  $N(E) \propto g(E)$  (Fig. 2A, inset) is in agreement with the  $N(E)$  first reported for LiFeAs (29, 30). It indicates (i) a fully gapped superconductor because  $g(E) \sim 0$  for  $|E| < 1$  meV, (ii) a maximum energy gap of  $\sim 6$  meV, and (iii) a complex internal structure to  $N(E)$  consistent with strong  $\vec{k}$ -space gap anisotropy.

Next, we image  $g(\vec{r}, E)$  in  $\sim 90$  nm square fields of view (FOV) at temperatures between 1.2 K and 16 K and in the energy range associated with Cooper pairing [(2), section VI]. The large FOV is required to achieve sufficient  $\vec{q}$ -space resolution. Figure 2, B and C, shows a typical  $g(\vec{r}, E)$  and its Fourier transform  $g(\vec{q}, E)$  with  $E = 7.7$  meV,

and the inset shows a typical  $\vec{r}$ -space example of the interference patterns. Figure 2, C and D, shows representative Fourier transforms  $g(\vec{q}, E)$  from energies above the maximum superconducting gap magnitude ( $E = +7.7$  meV,  $-6.6$  meV). The scattering interference signatures for three distinct bands can be detected as closed contours in  $\vec{q}$ -space; we refer to them as  $h_3$ ,  $h_2$ , and  $h_1$  throughout. The measured  $|\vec{q}|(E)$  of these bands in Fig. 2E shows them all to be hole-like. A quantitative comparison of QPI to both ARPES (15–17) and quantum oscillation measurements (31) [(2), section VII] identifies  $h_1$ ,  $h_2$ , and  $h_3$  with the three hole-like bands assigned  $\alpha_1$ ,  $\alpha_2$ , and  $\gamma$ . The QPI signatures of electron-like bands are weak and complex, perhaps because they share the same  $\vec{q}$ -space regions as the signature of  $h_2$ , or because of the stronger  $k_z$  dispersion of these bands, or because of weak overlap between high- $|\vec{k}|$  states and the localized tip electron wave function; we do not consider them further here.

Figure 3, A and B, shows the  $g(\vec{q}, E)$  measured within the energy gaps in Fig. 2E. Scattering interference is virtually nonexistent in the  $\vec{q}$ -space direction parallel to  $\Gamma\tilde{X}$  for the  $h_3$  band (Fig. 3A, green arrows) and is similarly faint in a direction parallel to  $\Gamma\tilde{M}$  for the  $h_2$  band (Fig. 3B, green arrows). The disappearance in the superconducting phase of QPI in these two directions is a result of an anisotropic gap opening at relevant  $\vec{k}$ -space locations on these bands (see insets in Fig. 3, A and B), as predicted from both the T-matrix and JDOS simulations in Fig. 1, E and F. Figure 3C shows  $g(\theta, E)$ , the strongly anisotropic scattering intensity versus angle in  $\vec{q}$ -space

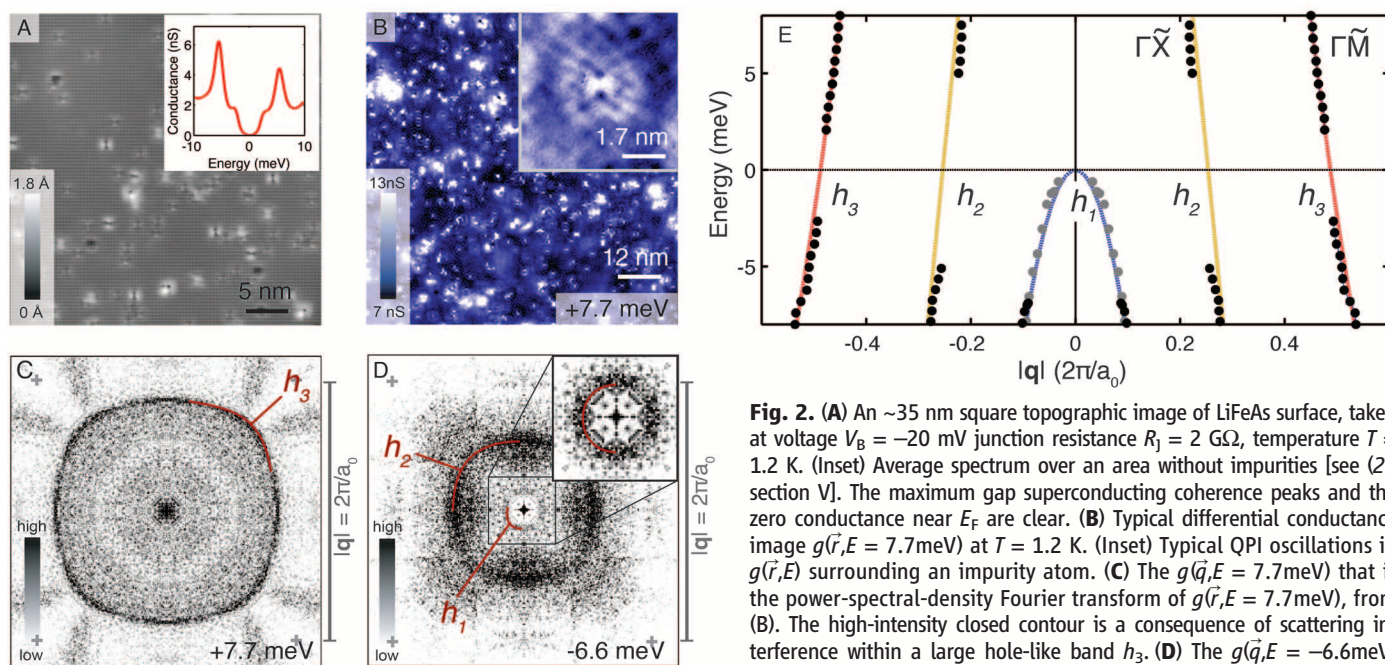


**Fig. 2.** (A) An  $\sim 35$  nm square topographic image of LiFeAs surface, taken at voltage  $V_b = -20$  mV junction resistance  $R_j = 2$  G $\Omega$ , temperature  $T = 1.2$  K. (Inset) Average spectrum over an area without impurities [see (2), section V]. The maximum gap superconducting coherence peaks and the zero conductance near  $E_F$  are clear. (B) Typical differential conductance image  $g(\vec{r}, E = 7.7$  meV) at  $T = 1.2$  K. (Inset) Typical QPI oscillations in  $g(\vec{r}, E)$  surrounding an impurity atom. (C) The  $g(\vec{q}, E = 7.7$  meV) that is the power-spectral-density Fourier transform of  $g(\vec{r}, E = 7.7$  meV), from (B). The high-intensity closed contour is a consequence of scattering interference within a large hole-like band  $h_3$ . (D) The  $g(\vec{q}, E = -6.6$  meV) showing the high-intensity closed contours resulting from scattering interference from a smaller hole-like band  $h_2$ , and  $h_1$  (inset). These data are measured at  $T = 1.2$  K. (E) The measured energy dependence of the  $|\vec{q}|(E) = 2\vec{k}$  ( $E$ ) for all three bands in  $h_1$  (blue line),  $h_2$  (yellow), and  $h_3$  (red) along the marked directions. Black dots are measured in the superconducting phase at  $T = 1.2$  K; gray dots are measured in the normal state at  $T = 16$  K.

interference from a smaller hole-like band  $h_2$ , and  $h_1$  (inset). These data are measured at  $T = 1.2$  K. (E) The measured energy dependence of the  $|\vec{q}|(E) = 2\vec{k}$  ( $E$ ) for all three bands in  $h_1$  (blue line),  $h_2$  (yellow), and  $h_3$  (red) along the marked directions. Black dots are measured in the superconducting phase at  $T = 1.2$  K; gray dots are measured in the normal state at  $T = 16$  K.

$g(\vec{q}, E)$  on the  $h_3$  Fermi surface. The  $g(\vec{q}, E)$  data in Fig. 3, A and B, together with the  $g(\theta, E)$  data in Fig. 3C, reveal unambiguous QPI signatures for anisotropic gaps of different orientations on different bands in LiFeAs.

To quantify the  $\Delta_i(\vec{k})$ , we examine the scattering intensity in  $g(\vec{q}, E)$  within a  $|\vec{q}|$ - $E$  plane defined first by  $\vec{q}$  parallel to  $\Gamma\tilde{M}$  and then by  $\vec{q}$

parallel to  $\Gamma\tilde{X}$ . The locus of maximum intensity in the  $g(|\vec{q}|, E)$  plane with  $|\vec{q}|$  parallel to the  $\Gamma\tilde{M}$  direction is extracted [(2), section VIII] and plotted in Fig. 3D. The evolution of the normal-state  $h_3$  band (red in Fig. 2E) is indicated here by red arrows. The superconducting energy gap minimum of  $h_3$  is seen, along with the curved trajectories of scattering intensity maxima ex-

pected from an anisotropic  $\Delta(\vec{k})$  (Fig. 1, G and H) [(2), section VIII]. Similarly, by measuring  $g(|\vec{q}|, E)$  in the plane with  $|\vec{q}|$  parallel to  $\Gamma\tilde{X}$ , the locus of maximum intensity of the  $h_2$  band is extracted [(2), section VIII] and plotted in Fig. 3E. The energy gap minimum is again obvious along with the curved scattering intensity maxima expected from a different anisotropic  $\Delta(\vec{k})$

**Fig. 3.** (A)  $g(\vec{q}, E = 2 \text{ meV})$  measured at  $T = 1.2 \text{ K}$ . The scattering on the  $h_3$  band has become highly anisotropic within its energy gap range, with vanishing intensity in the  $\Gamma\tilde{M}$  direction (green arrows). The inset shows schematically in  $k$ -space how this is indicative of a lower energy gap along  $\Gamma\tilde{M}$  and a higher energy gap along  $\Gamma\tilde{X}$ . (B)  $g(\vec{q}, E = -5 \text{ meV})$  measured at  $T = 1.2 \text{ K}$ . The scattering on the  $h_2$  band has become highly anisotropic within its energy gap range (green arrows), indicative of a lower energy gap along  $\Gamma\tilde{X}$  and a higher energy gap along  $\Gamma\tilde{M}$ . (C) A projection of the QPI intensity  $g(\vec{q}, E)$  (a three-dimensional data set) onto the measured normal-state band dispersion  $\varepsilon(\vec{k}) = \varepsilon(\vec{q}/2)$ . In the direction of minimal gap ( $\Gamma\tilde{M}$ ), the intensity is gapped up to around  $2 \text{ meV} \approx \Delta_{h_3}^{\min}$ , whereas in the direction of maximal gap ( $\Gamma\tilde{X}$ ), it is gapped up to around  $3 \text{ meV} \approx \Delta_{h_3}^{\max}$ . (D) Extracted maximum scattering intensity trajectory from  $g(|\vec{q}|, E)$  for  $\vec{q} \parallel \Gamma\tilde{X}$  [(2), section VIII] containing the information on  $\Delta(\vec{k})$  for  $h_3$ . (E) Extracted maximum scattering intensity trajectory from  $g(|\vec{q}|, E)$  for  $\vec{q} \parallel \Gamma\tilde{M}$  [(2), section VIII] containing the information on  $\Delta(\vec{k})$  for  $h_2$ . Blue: Gap opening on the  $h_1$  band.

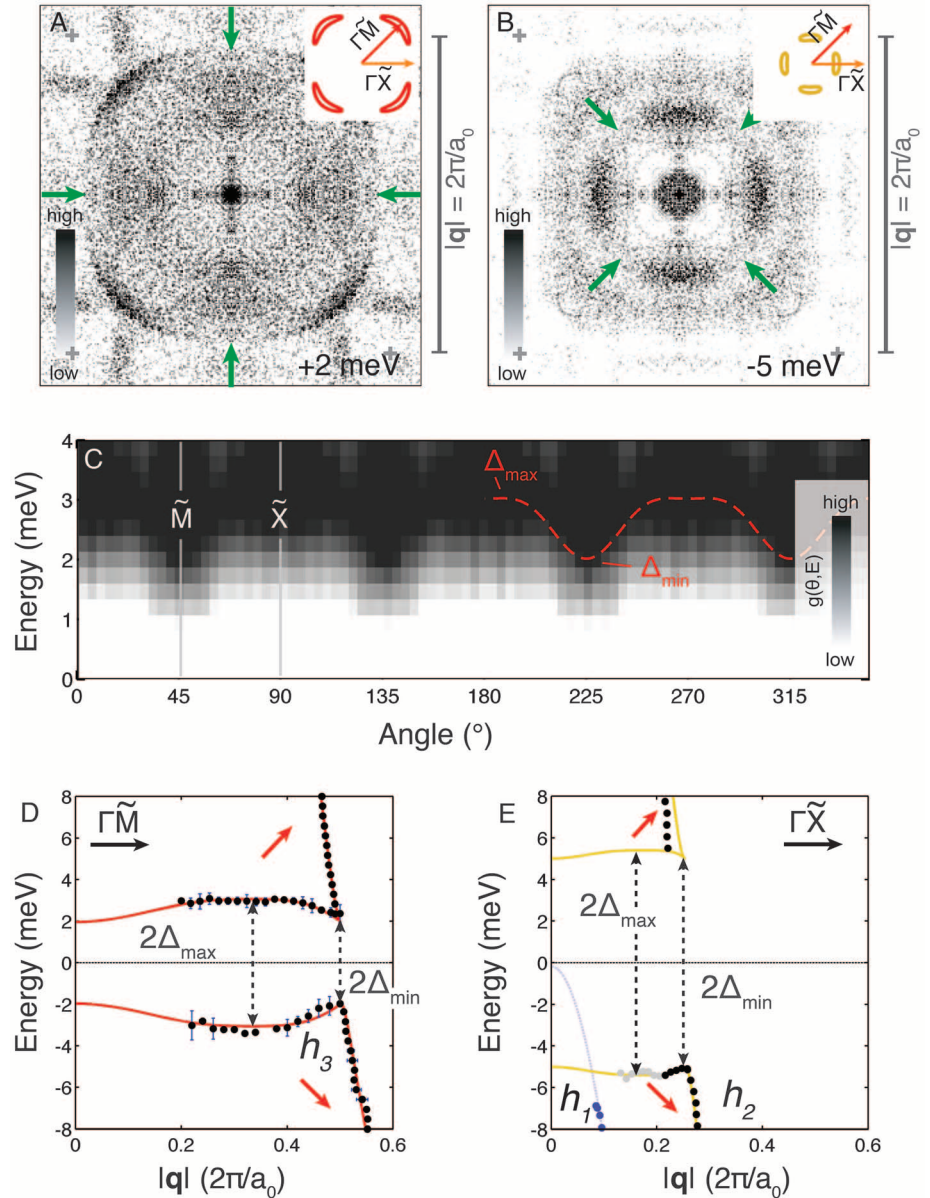
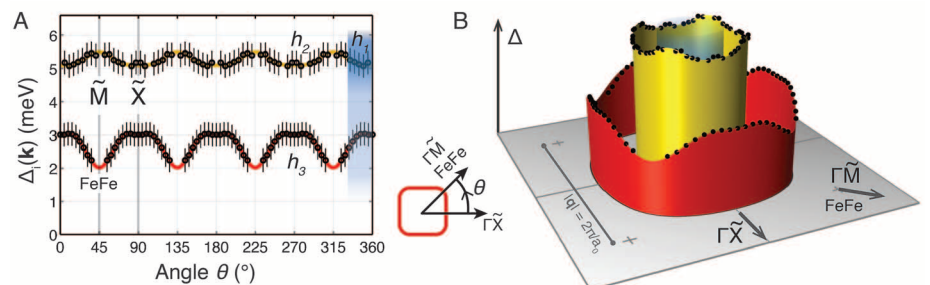


**Fig. 4.** (A) Anisotropic energy gap structure  $\Delta_i$  measured using QPI at  $T = 1.2 \text{ K}$  on the three hole-like bands  $h_3$ ,  $h_2$ , and  $h_1$  (Fig. 2E). These bands have been labeled  $\gamma$ ,  $\alpha_1$ , and  $\alpha_2$  before. Here, the  $0.35 \text{ meV}$  error bars stem from the thermal resolution of SI-STM at  $1.2 \text{ K}$ . (B) A three-dimensional rendering of the measured (solid dots) anisotropic energy gap structure  $\Delta$  on the three hole-like bands at  $T = 1.2 \text{ K}$ .





(see Fig. 1H); the data for the upper branch cannot be obtained because of interference from other signals (possibly the electron-like band). The QPI signature of the third band  $h_1$  becomes unidentifiable within  $-6 \pm 1.5$  meV below  $E_F$  in the superconducting phase, consistent with the opening of a gap of this magnitude (Figs. 2E and 3E), but we cannot yet resolve any gap modulations.

The magnitude, anisotropy, and relative position of  $\Delta_i(\vec{k})$  on bands  $h_3$ ,  $h_2$ , and  $h_1$  are then determined from Fig. 3, D and E, using the previously described procedure [(2), section III]. The resulting anisotropic superconducting gaps on bands  $h_3$ ,  $h_2$ , and  $h_1$  of LiFeAs are displayed in Fig. 4, A and B. Although our  $g(\vec{q}, E)$  agree well with pioneering QPI studies of LiFeAs where common data exist, no studies of  $\Delta_i(\vec{k})$  were reported therein (30). Moreover, although field-dependent Bogoliubov QPI can reveal OP symmetry (11), these techniques were not applied here to LiFeAs, and no OP symmetry conclusions were drawn herein. The anisotropic  $\Delta_i$  reported recently in ARPES studies of LiFeAs (16, 17) appear in agreement with our observations for the  $h_3$  (Fig. 1,  $\gamma$ ) and  $h_2$  (Fig. 1,  $\alpha_2$ ) bands. Lastly, our measurements are quite consistent with deductions on LiFeAs band structure from quantum oscillation studies (31). Overall, the growing confidence and concord in the structure of  $\Delta_i(\vec{k})$  for LiFeAs will advance the quantitative theoretical study of the mechanism of its Cooper pairing. Moreover, the multiband anisotropic-gap QPI techniques introduced here will allow equivalent  $\Delta_i(\vec{k})$  observations in other iron-pnictide superconductors.

## References and Notes

- P. J. Hirschfeld, M. M. Korshunov, I. I. Mazin, *Rep. Prog. Phys.* **74**, 124508 (2011).
- Materials and methods are available as supplementary materials on Science Online.
- F. Wang, H. Zhai, Y. Ran, A. Vishwanath, D.-H. Lee, *Phys. Rev. Lett.* **102**, 047005 (2009).
- T. A. Maier, S. Graser, D. J. Scalapino, P. J. Hirschfeld, *Phys. Rev. B* **79**, 224510 (2009).
- R. Thomale, C. Platt, J. Hu, C. Honerkamp, B. A. Bernevig, *Phys. Rev. B* **80**, 180505R (2009).
- S. Raghu, X.-L. Qi, C.-X. Liu, D. J. Scalapino, S.-C. Zhang, *Phys. Rev. B* **77**, 220503R (2008).
- R. Sknepnek, G. Samolyuk, Y.-B. Lee, J. Schmalian, *Phys. Rev. B* **79**, 054511 (2009).
- S. Maiti, A. V. Chubukov, *Phys. Rev. B* **82**, 214515 (2010).
- H. Kontani, S. Onari, *Phys. Rev. Lett.* **104**, 157001 (2010).
- A. D. Christianson *et al.*, *Nature* **456**, 930 (2008).
- T. Hanaguri, S. Niitaka, K. Kuroki, H. Takagi, *Science* **328**, 474 (2010).
- B. Zeng *et al.*, *Nat. Comm.* **1**, 112 (2010).
- J.-Ph. Reid *et al.*, *Phys. Rev. B* **82**, 064501 (2010).
- M. A. Tanatar *et al.*, *Phys. Rev. Lett.* **104**, 067002 (2010).
- S. V. Borisenko *et al.*, *Phys. Rev. Lett.* **105**, 067002 (2010).
- S. V. Borisenko *et al.*, *Symmetry* **4**, 251 (2012).
- K. Umezawa *et al.*, *Phys. Rev. Lett.* **108**, 037002 (2012).
- Q.-H. Wang, D.-H. Lee, *Phys. Rev. B* **67**, 020511R (2003).
- L. Capriotti, D. J. Scalapino, R. D. Sedgewick, *Phys. Rev. B* **68**, 014508 (2003).
- T. S. Nunner, W. Chen, B. M. Andersen, A. Melikyan, P. J. Hirschfeld, *Phys. Rev. B* **73**, 104511 (2006).
- Y.-Y. Zhang *et al.*, *Phys. Rev. B* **80**, 094528 (2009).
- A. Akbari, J. Knolle, I. Eremin, R. Moessner, *Phys. Rev. B* **82**, 224506 (2010).
- S. Sykora, P. Coleman, *Phys. Rev. B* **84**, 054501 (2011).
- I. I. Mazin, S. A. J. Kimber, D. N. Argyriou, *Phys. Rev. B* **83**, 052501 (2011).
- X. C. Wang *et al.*, *Solid State Commun.* **148**, 538 (2008).
- M. J. Pitcher *et al.*, *J. Am. Chem. Soc.* **132**, 10467 (2010).
- C. W. Chu *et al.*, *Physica C* **469**, 326 (2009).
- D. J. Singh, *Phys. Rev. B* **78**, 094511 (2008).
- T. Hanaguri *et al.*, *Meeting Abstracts of the Phys. Soc. of Japan*, **65**, 617 (2010).
- T. Hanke *et al.*, *Phys. Rev. Lett.* **108**, 127001 (2012).
- C. Putzke *et al.*, *Phys. Rev. Lett.* **108**, 047002 (2012).

**Acknowledgments:** We are particularly grateful to D.-H. Lee for advice and discussions, and we acknowledge and thank F. Baumberger, A. Carrington, P. C. Canfield, A. V. Chubukov, A. I. Coldea, M. H. Fischer, T. Hanaguri, P. J. Hirschfeld, B. Keimer, E.-A. Kim, M. J. Lawler, C. Putzke, J. Schmalian, H. Takagi, Z. Tesanovic, R. Thomale, S. Uchida, and F. Wang for helpful discussions and communications. Studies were supported by the Center for Emergent Superconductivity, an Energy Frontier Research Center, funded by the U.S. Department of Energy under DE-2009-BNL-PM015; by the UK Engineering and Physical Sciences Research Council (EPSRC); and by a Grant-in-Aid for Scientific Research C (no. 22540380) from the Japan Society for the Promotion of Science. Y.X. acknowledges support by the Cornell Center for Materials Research (CCMR) under NSF/DMR-0520404. T.-M.C. acknowledges support by Academia Sinica Research Program on Nanoscience and Nanotechnology, and A.P.M. the receipt of a Royal Society-Wolfson Research Merit Award. The data described in the paper are archived by the Davis Research Group at Cornell University.

## Supplementary Materials

www.sciencemag.org/cgi/content/full/336/6081/563/DC1  
Materials and Methods  
Supplementary Text  
Figs. S1 to S10  
References (32–36)

10 October 2011; accepted 3 April 2012  
10.1126/science.1218726

# Magnetic Reconnection in the Near Venusian Magnetotail

T. L. Zhang,<sup>1,2\*</sup> Q. M. Lu,<sup>1</sup> W. Baumjohann,<sup>2</sup> C. T. Russell,<sup>3</sup> A. Fedorov,<sup>4</sup> S. Barabash,<sup>5</sup> A. J. Coates,<sup>6</sup> A. M. Du,<sup>7</sup> J. B. Cao,<sup>8</sup> R. Nakamura,<sup>2</sup> W. L. Teh,<sup>2</sup> R. S. Wang,<sup>2</sup> X. K. Dou,<sup>1</sup> S. Wang,<sup>1</sup> K. H. Glassmeier,<sup>9</sup> H. U. Auster,<sup>9</sup> M. Balikhin<sup>10</sup>

Observations with the Venus Express magnetometer and low-energy particle detector revealed magnetic field and plasma behavior in the near-Venus wake that is symptomatic of magnetic reconnection, a process that occurs in Earth's magnetotail but is not expected in the magnetotail of a nonmagnetized planet such as Venus. On 15 May 2006, the plasma flow in this region was toward the planet, and the magnetic field component transverse to the flow was reversed. Magnetic reconnection is a plasma process that changes the topology of the magnetic field and results in energy exchange between the magnetic field and the plasma. Thus, the energetics of the Venus magnetotail resembles that of the terrestrial tail, where energy is stored and later released from the magnetic field to the plasma.

**M**agnetic reconnection is an important process in many astrophysical plasma environments, which leads to efficient and fast conversion of magnetic energy into kinetic energy of plasma particles. As a result of the rapid reconfiguration of the magnetic topology, it also transfers mass between different astrophysical plasma regimes. In particular, reconnection is associated with the formation of

solar coronal mass ejections (1) and plasmoid ejections from the magnetotails of Earth, Jupiter, Saturn, and Mercury (2–5), all of which lead to substantial plasma loss. Magnetic reconnection may also be responsible for comet tail disconnection, which releases much of a comet's plasma tail into space (6, 7). Although understanding atmospheric loss is a key to establishing the evolutionary history of planets, the role of magnetic

reconnection is still poorly understood because of the scarcity of in situ observations at planets other than Earth.

Three mechanisms of atmospheric loss have been identified at Venus:  $V \times B$  pick-up processes (where  $V$  is velocity and  $B$  is the magnetic field),  $J \times B$  acceleration in the plasma sheet (where  $J$  is current density), and the polar wind-type process in the tail boundary layer (8). Recent Venus Express data (9) reveal escape through the plasma sheet of the magnetotail and the tail boundary layer. Here, we show that reconnection is another acceleration mechanism, a situation not expected in the induced tail of Venus.

<sup>1</sup>Chinese Academy of Sciences Key Laboratory of Geospace Environment, University of Science and Technology of China, Hefei 230026, China. <sup>2</sup>Space Research Institute, Austrian Academy of Sciences, Graz 8042, Austria. <sup>3</sup>Institute of Geophysics and Planetary Physics, University of California, Los Angeles (UCLA), CA 90095–1567, USA. <sup>4</sup>Centre d'Etude Spatiale des Rayonnements, Toulouse 31028, France. <sup>5</sup>Swedish Institute of Space Physics, Kiruna 98128, Sweden. <sup>6</sup>Mullard Space Science Laboratory, University College London, London RH5 6NT, UK. <sup>7</sup>Institute of Geology and Geophysics, Chinese Academy of Sciences, Beijing 100029, China. <sup>8</sup>Space Science Institute, Beihang University, Beijing 100191, China. <sup>9</sup>Institut für Geophysik und Extraterrestrische Physik, Technische Universität Braunschweig, Braunschweig 38106, Germany. <sup>10</sup>Department of Automatic Control and Systems Engineering, University of Sheffield, Sheffield S1 3JD, UK.

\*To whom correspondence should be addressed. E-mail: tielong.zhang@oeaw.ac.at